

1 **Separate Zones of Sulfate and Sulfide Release from Subducted Mafic Oceanic Crust**

2
3
4
5
6

Andrew G. Tomkins¹ and Katy A. Evans²

- 7 1. School of Earth, Atmosphere and Environment, Monash University, Melbourne, Victoria
8 3800, Australia
- 9 2. School of Applied Geology, Curtin University, GPO Box 1987, WA6845, Australia

10
11
12

13 *Corresponding Author Details:

14 Andrew Tomkins
15 Email: andy.tomkins@monash.edu
16 Phone: +61 3 9905 1643
17 Fax: +61 3 9905 4903

18

19 Keywords: Sulfur, sulfate, sulfur cycle, subduction, arc magmatism, porphyry copper

20
21

22 **Abstract**

23 Liberation of fluids during subduction of oceanic crust is thought to transfer sulfur into the overlying
24 sub-arc mantle. However, despite the importance of sulfur transfer in magmatic arcs to diverse
25 processes ranging from climate change to magma oxidation and ore formation, there has been little
26 investigation of the metamorphic reactions responsible for sulfur release from subducting slabs. Here,
27 we investigate the relative stability of anhydrite (CaSO_4) and pyrite (FeS_2) in subducted basaltic
28 oceanic crust, the largest contributor to the subducted sulfur budget, to place constraints on the
29 processes controlling sulfur release. Our analysis of anhydrite stability at high pressures suggests that
30 this mineral should dominantly break down across a narrow temperature interval at the transition from
31 blueschist to eclogite facies, particularly at higher pressures. In contrast, pyrite appears to be
32 conserved well into the eclogite facies, as indicated by the preservation of pyrite-bornite inclusions in
33 coesite-bearing eclogites from the Sulu Belt in China, which reached temperatures of at least 750°C .
34 Given that eclogite xenoliths from diamond-bearing kimberlites, which experienced much higher
35 temperatures, contain only pyrrhotite (FeS), we suggest that sulfur release via conversion of pyrite to
36 pyrrhotite occurs at temperatures above 750°C . Thus, sulfur may be released from subducting slabs
37 in two separate pulses; the first releasing varying proportions of SO_2 , HSO_4^- and H_2S via anhydrite
38 breakdown at the blueschist-eclogite transition, promoting oxidation of remaining silicates in some
39 domains, and the second releasing H_2S via pyrite breakdown well into the eclogite facies, which may
40 in some circumstances coincide with slab melting or supercritical liquid generation driven by influx of
41 serpentinite-derived fluids. These results imply that the metallogenic potential in the sub-arc mantle
42 above the subducting slab varies as a function of subduction depth, having the greatest potential
43 above the blueschist-eclogite transition given the association between oxidised magmas and
44 porphyry Cu(-Au-Mo) deposits. We speculate that this zoned sulfur liberation might be one of the
45 factors that lead to the apparently redox-influenced zoned distribution of ore deposit types in the
46 Andean arc. Furthermore, given the lack of sulfate-associated sea floor oxidation prior to the second
47 great oxidation event, the pattern of sulfur transfer from the slab to the sub-arc mantle likely changed
48 over time, becoming shallower and more oxidized from the Neoproterozoic onwards.

49
50

51 **Introduction**

52

53 Sulfur is an abundant environment-influencing element that has played a key role in the
54 evolution of life, and is a fundamental component of subduction-related ore-forming systems.
55 Subduction of oceanic crust brings sulfur from the near-surface into the deep Earth, where
56 metamorphism promotes further migration from the slab into the overlying sub-arc mantle
57 (e.g., Richards, 2011), which is the ultimate source of metals for many of the world's largest
58 ore deposits. However, there is little understanding of how the key sulfur-bearing minerals,
59 pyrite (FeS_2) and anhydrite (CaSO_4), behave during subduction zone metamorphism, so
60 controls on the spatial and temporal distribution of sulfur liberation from the slab are poorly
61 constrained.

62

63 Magmatic arcs contain numerous ore deposits, which collectively represent our main
64 source Cu and Mo, and a major source of Au (e.g., Richards, 2011). Some continental arcs
65 have zoned metal distribution. In the Andes, in the vicinity of Chile, Bolivia and Argentina,
66 the near-trench arc in the west contains gigantic porphyry $\text{Cu}\pm\text{Mo}\pm\text{Au}$ and epithermal $\text{Au}+\text{Ag}$
67 deposits, whereas to the east, further away from the trench, is a belt of pluton-related Sn-
68 polymetallic and intrusion-related/orogenic gold deposits (Figure 1). The oxidation state of
69 felsic intrusions associated with these deposits also varies as a function of trench proximity;
70 the near-trench porphyry Cu-associated intrusions tend to be oxidised (e.g., Richards, 2011),
71 whereas those associated with the trench-distal deposit types tend to be reduced (Lang and
72 Baker, 2001). It is generally accepted that magma oxidation state strongly influences the
73 genesis of arc-related ore deposits (e.g., Richards, 2009; 2011). Although there is
74 considerable discussion at present (e.g., Cottrell and Kelley, 2011; Lee et al., 2010; Mallmann
75 and O'Neill, 2009), some evidence favours the hypothesis that magma oxidation state is
76 inherited from processes that occur in the mantle wedge above the subducting oceanic slab

77 (e.g., Evans et al., 2012; McInnes et al., 2001). A significant proportion of this mantle wedge
78 oxidation may evolve through addition of slab-derived sulfate (Evans and Tomkins, 2011) via
79 fluids that also carry other elements that are typically enriched in arc magmas.

80

81 Most mineral deposits found in magmatic arcs could not form without sulfur because it is
82 a complexing ligand for aqueous transport of some metals, and a necessary co-precipitant for
83 others. Oxidation state controls the nature of the chemical compounds that sulfur can form,
84 and thus redox processes regulate sulfur-associated metal mobilisation, transport and
85 deposition. For example, sulfide is an order of magnitude less soluble in basaltic melt than
86 sulfate (Jugo et al., 2010), which thus influences the uptake of metals into basaltic magma
87 during partial melting of the mantle wedge and during upward migration of arc magmas
88 through the crust (Jenner et al., 2010; Tomkins et al., 2012). It is therefore important to
89 understand the metamorphic reactions that release sulfur from the subducting oceanic slab,
90 and the controls on sulfur redox state.

91

92 As metasomatised oceanic crust is subducted into the mantle at convergent margins, it is
93 subjected to high pressure – low temperature metamorphism. As metamorphism progresses,
94 pore water and exchangeable water are driven off at relatively shallow depths, and then
95 structurally bound water is liberated by a series of progressive metamorphic reactions as the
96 slab P-T conditions increase from prehnite-pumpellyite to blueschist to eclogite facies. In this
97 process hydrated silicates such as chlorite, glaucophane and lawsonite (in blueschists) are
98 converted to anhydrous garnet and omphacite (in eclogites). The metamorphic reactions
99 between silicate minerals are well understood, but there has been minimal research on the
100 metamorphic controls on sulfur-liberation from the slab prior to melting.

101

102 Here, we investigate the metamorphic processes that control sulfur liberation from
103 subducting oceanic crust, in order to place constraints on the global sulfur cycle and on ore
104 genesis. Basaltic oceanic crust provides the biggest contribution to the subduction zone sulfur
105 cycle (Evans et al., 2012; Evans and Tomkins, 2011), so this paper focuses on sulfur-bearing
106 mineral stability during subduction zone metamorphism of oceanic basalts. We firstly review
107 the current understanding of the distribution of sulfur within the basaltic oceanic crust prior
108 to subduction, before examining the metamorphic stability of two key minerals, anhydrite
109 and pyrite. Thermodynamic modeling is used to investigate anhydrite dissolution in fluids
110 produced by progressive slab metamorphism. Observations of sulfide inclusions in eclogitic
111 garnet are used to place some constraints on pyrite stability. Our results suggest that sulfur
112 may be released from subduction zones initially as sulfate at shallower levels, and then as
113 sulfide at deeper levels.

114

115

116 **Pre-metamorphic Sulfur Addition to the Oceanic Crust**

117

118 In the modern Earth, sulfur is mainly dissolved in seawater as sulfate, which is the
119 second most abundant anion after Cl⁻. Unaltered mid-ocean ridge basalt (MORB) typically
120 has a primary sulfur content of 950 to 1450 ppm (Jenner et al., 2010), mainly in the form of
121 reduced magmatic sulfide (pyrrhotite – Fe_{1-x}S, chalcopyrite – CuFeS₂, pentlandite –
122 (FeNi)₉S₈, and bornite – Cu₅FeS₄ in some cases). Prior to subduction, mafic oceanic crust
123 becomes metasomatised at two main localities: (1) at mid-ocean ridges and ridge flanks,
124 active rifting and high heat flow combine to promote downward seawater circulation into the
125 upper oceanic crust, some of which is later expelled at black smoker chimneys close to the
126 ridge axis (Fig. 2; e.g., Hannington et al., 2005); (2) at the pre-trench bend in the oceanic

127 crust, normal faulting allows draw down of seawater into the oceanic crust (Faccenda et al.,
128 2009). During this metasomatic alteration the upper oceanic crust initially reacts with
129 oxidised sulfate-bearing seawater to transform the primary sulfides into a secondary sulfide
130 assemblage, which varies as a function of oxidation state (Alt et al., 2010; Alt and Shanks,
131 2011; Barker et al., 2010; Staudigel, 2003). Pyrrhotite may be transformed into pyrite, and
132 chalcopyrite, although typically retained, can be converted to bornite (Alt, 1989). Pentlandite
133 is common in the secondary sulfide assemblage, and millerite (NiS) has also been observed
134 (Alt, 1989). These authors also observed sphalerite and galena (PbS) in the secondary sulfide
135 assemblage.

136

137 This sulfate reduction drives iron oxidation, and seawater infiltration is commonly
138 associated with increased $\text{Fe}^{3+}/\Sigma\text{Fe}$ and hematite formation (Barker et al., 2010). More
139 extensive infiltration and reaction precipitates anhydrite (CaSO_4) over the temperature range
140 36 – 408°C (Alt et al., 2010; Hannington et al., 2005). The oceanic crust is somewhat
141 vertically zoned in its sulfur-bearing mineral distribution, varying as a function of extent of
142 seawater infiltration and temperature, such that lateral variation is controlled by extent of
143 faulting and intrinsic permeability; e.g., sheeted dykes have high vertical, but poor lateral
144 permeability. The most oxidised alteration containing anhydrite and pyrite occurs in zones
145 that experienced the highest fluid:rock ratios, becoming pyrite-dominated at deeper levels of
146 more reduced alteration, and progressing to pyrrhotite-dominated in the deepest, least altered,
147 most reduced regions (Alt, 1995). However, because anhydrite solubility decreases with
148 increasing temperature, this mineral appears to be enriched in zones where cool sulfate-
149 bearing seawater mixes with ascending hotter basement fluids, such as the upper part of the
150 sheeted dyke complex (Alt et al., 2010). A significant proportion of H_2O is also added to the
151 upper oceanic crust (~10 wt.% of the upper crust), in the form of pore water, exchangeable

152 water (within clays and zeolites), and structurally bound water (in hydrated silicate minerals)
153 (Staudigel, 2003).

154

155 Data on the sulfate concentration in altered oceanic crust are sparse. Information
156 provided by Alt and Shanks (2011) indicates that uppermost oceanic crust lavas in IODP Hole
157 1256D contain an average of 125 ppm S^{6+} , which equates to 0.053 wt.% anhydrite, but the
158 sulfate and total sulfur content varies widely ($SO_4/\Sigma S = 0.047 - 0.882$; total S = 15 – 3120
159 ppm). Alt et al. (2010) reported that the upper part of the sheeted dyke complex in this same
160 IODP hole contains visible anhydrite in veins, purportedly indicating an enriched zone, but
161 did not report any compositional data. Barker et al. (2010) found that although the sheeted
162 dykes at Pito Deep (Easter Microplate) contained hydrothermal pyrite, sulfate was only
163 detected in one sample (100 ppm sulfate). These authors nevertheless suggested that their
164 geochemical data indicated anhydrite precipitation elsewhere in the Pito Deep system. These
165 studies commonly report extensive sulfur loss from some parts of the system and strong sulfur
166 enrichment in some samples (Alt, 1989, 1995; Barker et al., 2010), and cannot record the full
167 extent of sulfur addition prior to deep subduction. Further hydration of the crust occurs at the
168 slab bend (Faccenda et al., 2009), which would drive additional sulfate-related alteration, and
169 there is huge variability in sulfide/sulfate concentration as represented by mineral deposits.
170 Evans et al. (2012) estimated the S^{6+} content of typical subducted MORB at 0.037 wt.%
171 (uncertainty estimated at 50%), although this is a rudimentary estimate based on few data.
172 This value equates to 0.157 ± 0.079 wt.% anhydrite.

173

174 **Thermodynamic Modelling of Anhydrite Dissolution in Metamorphic Fluids**

175

176 To investigate sulfur liberation from anhydrite during progressive metamorphism we
177 combined Perple_X modeling of H₂O production during subduction of hydrated MORB
178 basalt with calculations of variations in anhydrite solubility as a function of pressure and
179 temperature. A P-T pseudosection was generated using Perple_X 6.7.1 (Connolly, 2005) in
180 the system Na₂O-CaO-FeO-MgO-Al₂O₃-SiO₂-H₂O for an N-MORB composition derived
181 from the MAR N-MORBS (Table 1). K₂O was omitted because it is present in low
182 concentrations in N-MORB bulk compositions and minimally affects the water budget during
183 devolatilisation. Similarly, ferric iron was omitted because the stabilisation of small amounts
184 of oxide phases, such as magnetite, has little effect on the overall water budget. It is
185 emphasised that the purpose of the thermodynamic modeling is to simulate water release on
186 hot and cold subduction geotherms; second order details of phase diagram topology and phase
187 compositions are not of primary interest, and do not affect the results or conclusions.

188

189 We used the hp02ver.dat data file, which contains an updated version of the Holland and
190 Powell (1998) dataset. Mineral phases included, and the relevant activity composition models
191 were: orthopyroxene (Powell and Holland, 1999); chlorite (after Holland et al., 1998);
192 omphacitic clinopyroxene (Holland and Powell, 1996); garnet (Holland and Powell, 1998);
193 plagioclase feldspar (Fuhrman and Lindsley, 1988); chloritoid (symmetric non-ideality with a
194 w_{FeMg} of 1 kJ mol⁻¹), talc (ideal), amphibole (Dale et al., 2005) and the pure phases lawsonite,
195 zoisite, water, quartz, and coesite. Thermodynamic properties for water were described using
196 the CORK equation of state (Holland and Powell, 1998).

197

198 This combination of activity-composition models was mostly taken from the Holland and
199 Powell (HP) models developed at around the same time as the HP98 dataset (Holland and
200 Powell, 1998), and are therefore compatible with this dataset. An exception is the feldspar

201 model (Fuhrman and Lindsley, 1988), which has been combined with the HP $a-x$ models
202 before (e.g., Connolly, 2005), produces results similar to the HP models, and is applicable
203 over a wider compositional range. A range of alternative $a-x$ models were tested and the
204 results compared with published THERMOCALC-derived pseudosection calculations.
205 Different combinations of activity-composition models produced different topologies for
206 areas of the diagram away from the subduction geotherms. However, the essential features of
207 interest for this study, that is, the pattern of water release and dehydrating minerals, were
208 consistent across a wide range of activity-composition models. Similarly, changes in the local
209 topology did not affect the positions of the main metamorphic facies, which are consistent
210 with the literature, although published pseudosections depicting assemblages at > 2 GPa are
211 not available for comparison, and natural data for verification of assemblages > 3 GPa are
212 sparse. Nevertheless, most of the dehydration reactions that extend to > 2 GPa that are found
213 at lower pressures, so we are confident of the broad pattern and absolute magnitudes of water
214 release.

215

216 In places, two clinopyroxenes (diopside and omphacite) are predicted due to the existence
217 of solvi in clinopyroxene composition space. The different cpx compositions have not been
218 distinguished on the pseudosections, for clarity. Similarly, two amphiboles coexist in a
219 number of fields. These are sodic amphiboles with glaucophane compositions stable at high
220 pressure and low temperature, calcic amphiboles (actinolites) stable at low pressure and
221 temperature, and Al-bearing amphiboles (hornblendes) stable at higher temperatures and
222 moderate pressure. Given that the pseudosection was generated to quantify water release on
223 subduction geotherms, the amphiboles are labeled as amph, for simplicity.

224

225 Water contents were calculated using WERAMI (Connolly, 2005) on a 100 x 100 grid
226 from 300 to 800°C and 1 to 5 GPa, and contoured using PSTABLE (Connolly, 2005). Figure
227 3 shows a P-T pseudosection calculated for hydrated typical N-MORB, with contours of H₂O
228 release. It can be seen that the majority of H₂O release occurs with the sequential loss of
229 chlorite, talc and amphibole.

230

231 Experimental work at 600–900°C and 0.6–1.4 GPa revealed that anhydrite solubility in
232 H₂O is strongly affected by pressure and salinity (Newton and Manning, 2005). At low
233 temperature anhydrite solubility decreases with increasing T, whereas the Newton and
234 Manning experiments showed that elevated pressure, solubility increases with both T and P.
235 Additionally, anhydrite solubility increases greatly with increasing salinity. We used the
236 expression, referred to here as NM05, provided by Newton and Manning (2005) to calculate
237 anhydrite solubility as a function of T, P and salinity. Anhydrite dissolution was then
238 calculated using the H₂O contents derived from the Perple_X modeling. Solubilities predicted
239 by NM05 are very high at the highest pressures considered, and, given the restricted range of
240 pressure over which the expression is calibrated, there is doubt as to whether these
241 solubilities are realistic, although Newton and Manning (2005) suggested that sulfate-salt-
242 rich solutions may exist in subduction zones. Nevertheless, a cautious approach has been
243 taken here and we have disregarded results that predict solubilities higher than 3 molar. This
244 approach does not limit the conclusions of the study, since the proportion of anhydrite
245 estimated to be present in typical MORB is dissolved long before these high solubilities are
246 approached.

247

248 NM05 is derived from experiments where oxygen fugacity was buffered by anhydrite
249 dissolution, which the authors indicated was between the SO₂-H₂S equivalence point and the

250 hematite-magnetite buffer. Anhydrite solubility is thought to increase moderately with
251 decreasing fO_2 , its dissolution generating mainly SO_2 at the hematite-magnetite (HM) buffer,
252 even proportions of H_2S and SO_2 slightly above the pyrite-pyrrhotite-magnetite (PPM)
253 buffer, and dominantly H_2S as fO_2 becomes progressively more reduced (Newton and
254 Manning, 2005). Two end-member salinities were used in our calculations, 4 and 10 wt%
255 NaCl. These salinities are based on the estimated range in salinities of fluids released by
256 dehydration of mafic blueschists (see review by Richards, 2011). The resulting data, in grams
257 $CaSO_4$ dissolved per kilogram of rock, were contoured and overlaid on the P-T
258 pseudosection.

259

260 Figures 4A and B show the same P-T pseudosection as Figure 3, with contours of
261 anhydrite dissolution in H_2O , containing 4 and 10% NaCl respectively, in a closed system
262 with anhydrite in excess. It can be seen that the amount of anhydrite dissolved in the fluid
263 increases significantly as chlorite, and then talc and the amphiboles (i.e., the hydrous
264 minerals), are consumed. Higher dP/dT trajectories (i.e., colder slabs) can dissolve
265 considerably more anhydrite at any given temperature. This affect is caused by the increase
266 in anhydrite solubility with pressure. Salinity has a significant effect; 10 wt% NaCl fluids
267 dissolve more anhydrite than 4 wt% NaCl fluids by a factor of up to 3. At the highest P and
268 T, the silicate assemblages are anhydrous, and so no new water is produced during
269 progressive metamorphism. Therefore, the increase in anhydrite dissolution seen in this
270 region is due to changes in solubility as a function of pressure and temperature, rather than
271 being driven by fluid production; i.e., the model assumes that the fluid stays in the rock and is
272 able to continuously dissolve more anhydrite as temperature and pressure increase.

273

274 Calculations for a quasi-open system were performed by splitting the cold and hot
275 geotherms shown in [Figure 4](#) into 100 increments, and calculating the mass of water lost on
276 each step using the NM05 expression ([Fig. 5A and B](#)). An exemplar for a periodically open
277 system was modeled using the same approach, but with water extraction only at the terminus
278 points of chlorite and talc break down ([Fig. 5C](#)). The closed and open system calculations are
279 similar at low temperatures, but diverge as water release slows and ceases when the
280 assemblage becomes anhydrous. The expected average quantity of anhydrite is, however,
281 completely dissolved in the quasi-open system – the most conservative system – at
282 temperatures ranging from 420°C on the cold geotherm to 625°C on the hot geotherm.

283

284 **Observations of Pyrite Inclusions in Eclogitic Garnet**

285

286 Pyrite has been recorded in equilibrium with eclogite facies silicate assemblages in samples
287 from New Caledonia ([Evans et al., 2014](#)), the Zermatt-Saas (Fee) Ophiolite Belt in Italy and
288 Switzerland ([Evans et al., 2014](#); [Giacometti et al., 2014](#)). These sample localities record a
289 range of metamorphic peak conditions from 600°C, 1.9 GPa in New Caledonia (see
290 references in [Evans et al., 2014](#)) to 600–630°C, 2.7–2.9 GPa at Lago de Cignana (coesite
291 present; [Reinecke, 1998](#)). Here, we discuss pyrite-bearing assemblages from the highest
292 temperature eclogites in the Sulu Belt, China, which are estimated to have reached PT
293 conditions of $755 \pm 55^\circ\text{C}$ and ~ 4 GPa ([Zhang et al., 2009](#)).

294

295 The Sulu Belt is the northeastern extension of the Dabie-Sulu collisional belt, which
296 represents a Triassic continent-continent collision zone. The samples for this study were
297 obtained from the eastern Jiaodong peninsula where the Sulu Belt abuts the eastern margin of
298 the North China Craton. Here, supracrustal and mafic-ultramafic rocks were subjected *in situ*

299 subduction-zone UHP metamorphism at depths of ~135 km before being exhumed (Zhang et
300 al., 2009 and references therein).

301

302 The samples from the Sulu Belt range from moderately coarse-grained garnet-omphacite
303 assemblages to eclogites with extremely coarse-grained garnet crystals up to 10 cm across.
304 Pyrite commonly forms on the retrograde path in eclogites (Evans et al., 2014), in which case
305 it forms on fluid pathways along grain boundaries between the silicates minerals, or
306 occasionally on cracks within silicates. Large garnet crystals are ideal for studying pre-
307 subduction sulfide assemblages, such as those formed during sea-floor alteration, because
308 early sulfides are incorporated into garnet as sub-spherical to negative crystal inclusions
309 during prograde metamorphism, allowing them to be distinguished from retrograde sulfide
310 minerals. The negative crystal shape of the sulfide inclusions indicates textural equilibration
311 with the surrounding garnet at high temperature and pressure (i.e., polysulfide inclusions
312 replicate the hexoctahedral garnet crystal shape). The large garnets from the Sulu Belt
313 contain numerous approximately hexagon-shaped inclusions of bornite ± pyrite ± covellite ±
314 chalcopyrite ± pentlandite ± an unidentified Te phase; these are pre-peak metamorphic
315 sulfides that equilibrated with the garnet as it grew. They are compositionally dominated by
316 bornite (many appear to be bornite-only in 2-dimensional thin sections); pentlandite is
317 moderately common, and pyrite is relatively rare. Pyrrhotite was not observed in any of the >
318 40 sulfide inclusions that we examined. Most of the polysulfide inclusions that lack pyrite are
319 free of radial cracks, whereas rare pyrite-bearing bornite inclusions have short radial cracks
320 that are filled with a thin film of bornite (Fig. 6A and B). Electron microprobe mapping of
321 several sulfide mineral inclusions indicates that major cations in the garnet preserve no
322 zoning relationship to the inclusions (Figs. 6C and D). These Sulu Belt polymineralic sulfide
323 inclusions are interpreted as sea-floor altered primary magmatic sulfides because of their Cu-

324 Ni-Fe-S composition; these are typical of magmatic sulfides (Jenner et al., 2010), whereas
325 sulfide grains associated with migration of subduction zone fluids are typically pyrite-only
326 (Evans et al., 2014).

327

328

329

DISCUSSION

330

331 **On the stability of anhydrite**

332 As the slab is subducted and starts to undergo metamorphism, pore water and
333 exchangeable water are released over the temperature interval 100–250°C. This initial water
334 flux would likely dissolve some anhydrite, since it has high solubility at low temperature and
335 pressure. Given that hematite is commonly associated with anhydrite in sea floor alteration
336 zones (Barker et al., 2010), most anhydrite-bearing rocks are expected to be sufficiently
337 oxidized for the dissolved sulfur species to be SO₂-dominated at these low grade conditions.
338 As this liberated fluid migrates upwards, it heats up because the slab is being heated by
339 surrounding warmer mantle. Since anhydrite has retrograde solubility at low pressures
340 (Newton and Manning, 2005), this heating would cause anhydrite to precipitate in veins
341 towards the top of the slab. As higher pressure conditions are reached with continued
342 subduction, anhydrite changes from having retrograde to prograde solubility, and this change
343 happens at depths where structurally bound water is starting to be released by metamorphic
344 reactions amongst the silicate minerals.

345

346 Various studies of blueschist facies rocks have found that a variety of oxidation states are
347 likely to exist within any given a package of subducting rocks. Blueschists in the Tavsanli
348 area of Northwest Turkey have either hematite-, hematite-magnetite- or magnetite-bearing

349 assemblages, most of which are hematite-bearing (Okay, 1980). A similar variety of fO_2
350 buffering assemblages has been found in other blueschists (Cotkin, 1987), and it seems that
351 hematite is a common, although not ubiquitous, constituent of blueschists in general.
352 Transitional eclogites, in contrast, commonly contain rutile, occasionally ilmenite and no
353 magnetite, because iron partitions into garnet and clinopyroxene as temperature and pressure
354 increase (Banno and Green, 1968; Frost, 1991); they are thus typically only weakly magnetic
355 (Liu et al., 2012). Thus in these rocks, oxygen fugacity would be buffered primarily by the
356 ferromagnesian silicates, which inherit elevated $Fe^{3+}/\Sigma Fe$ through consumption of hematite
357 and magnetite on the prograde path: Banno and Green (1968) showed experimentally that as
358 rocks evolve into the eclogite facies, Fe^{3+} is incorporated from magnetite into omphacite as
359 the acmite component, $NaFe^{3+}Si_2O_6$. Thus, although the oxidation state of natural iron oxide-
360 free transitional eclogites is poorly established, it is expected to range from above the
361 hematite-magnetite buffer for rocks that were heavily oxidised in the sea floor, down to
362 ~FMQ, the typical oxidation state of unaltered MORB basalts (Cottrell and Kelley, 2011).
363 Some high Fe-Ti eclogites contain evidence that ilmenite-hematite solid solution existed
364 during peak metamorphism (Liu et al., 2012), indicating oxygen fugacity conditions
365 immediately below the hematite-magnetite buffer (Frost, 1991). The sulfur species resulting
366 from anhydrite dissolution can range from mostly SO_2 with minor HSO_4^- at the hematite-
367 magnetite buffer, to equal proportions of SO_2 and H_2S at the pyrite-anhydrite buffer, and to
368 almost entirely H_2S at oxidation states equivalent to the NNO and FMQ buffers (see Fig. 5 in
369 Newton and Manning, 2005).

370

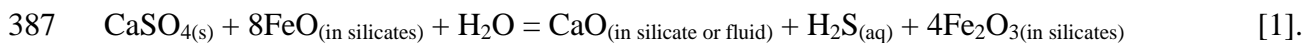
371 Figures 4 and 5 show that although some anhydrite dissolution may begin in the lower
372 blueschist facies, the greatest potential for dissolution exists across the blueschist-eclogite
373 transition; i.e., the zone where chlorite, talc and amphiboles are converted to the anhydrous

374 eclogite assemblage. This dissolution is particularly enhanced at higher pressures. Our
375 calculations indicate that for typical slab fluids about 0.1–0.6 wt.% (1–6 g/kg) anhydrite
376 would be dissolved across the transition into the eclogite facies, depending on the geothermal
377 gradient. Given the [Evans et al. \(2012\)](#) estimate that typical oceanic crust contains $0.157 \pm$
378 0.079 wt.% anhydrite, it is likely that all or nearly all anhydrite would be dissolved in the
379 metamorphic fluids generated at the blueschist-eclogite transition, without requiring any fluid
380 focusing.

381

382 The oxidation state and thus composition of the fluid produced by anhydrite dissolution is
383 controlled by equilibration between the fluid and the ferromagnesian silicate assemblage, the
384 iron-bearing oxide minerals and pyrite if present. In cases where the bulk oxidation state is
385 sufficiently reduced, significant H_2S would be generated by reactions such as:

386



388

389 This reaction results in oxidation of the silicate assemblage, but the oxidation effect can only
390 be small if the proportion of anhydrite in the rock is low. As such the silicate-sulfide-oxide
391 assemblage would overwhelm the buffering capacity of the anhydrite in most reduced rocks.
392 Nonetheless, only relatively small shifts in silicate $\text{Fe}^{3+}/\text{Fe}^{2+}$ are needed to produce moderate
393 changes in the bulk oxidation state. This is important because the solubility of sulfur in
394 subsequent slab-derived melt increases by an order of magnitude from FMQ+0.5 to
395 FMQ+1.5 ([Jego and Dasgupta, 2014](#); [Jugo et al., 2010](#)), which has significant consequences
396 for the metallogensis of arc magmas ([Jenner et al., 2010](#); [Tomkins et al., 2012](#)). Conversion
397 of sulfate to sulfide is an eight-electron change, so given appropriate conditions, reduction of
398 one mole of sulfate can oxidise eight moles of Fe^{2+} to Fe^{3+} . Given that eclogites inherit

399 elevated $\text{Fe}^{3+}/\Sigma\text{Fe}$ through equilibration with magnetite on the prograde path, many will have
400 $f\text{O}_2$ in the range FMQ+0.5 to +1.5 as anhydrite starts to break down, where only small
401 increases in $f\text{O}_2$ make a large difference in S solubility in later slab-derived melts (Fig. 7).
402 Thus we conclude that anhydrite breakdown at the blueschist-eclogite transition can make a
403 big difference in the fertility of later slab-derived melts.

404

405 In situations where sulfate is not reduced, SO_2 and minor HSO_4^- may escape the sites of
406 anhydrite dissolution to migrate upwards through the slab and potentially into the sub-arc
407 mantle. There is some evidence that the sub-arc mantle has been oxidised by fluids escaping
408 from the subducted slab (McInnes et al., 2001), and sulfate is thought to be the most likely
409 oxidant (Evans and Tomkins, 2011).

410

411 *Open System Processes*

412 Intermediate depth earthquakes are thought to be caused by increased fluid pressures
413 resulting from dehydration in the subducting slab (e.g., Moreno et al., 2014). Fluid-triggered
414 earthquakes will occur when fluid pressure approaches lithostatic pressure, and so a certain
415 amount of fluid-generating reaction needs to progress before an earthquake can be initiated.
416 Analysis of seismological data has been used to suggest that semi-continuously slipping
417 aseismic domains within broad areas of subducting slab are those with the highest
418 metamorphic fluid production (the easiest to fail), whereas those that rarely slip and produce
419 the largest earthquakes are the driest (Moreno et al., 2014). Thus the frequency of slip is
420 expected to correlate with the extent of prior sea floor metasomatism. Once an earthquake
421 occurs, numerous linking fractures develop that allow the fluid pressure to dissipate back to
422 the equilibrium state. So earthquakes are the trigger for fluid migration. Small slip events
423 form small fracture arrays; large earthquakes form regionally extensive networks of

424 connected faults and fractures where aftershocks are triggered by infiltration of new fluid via
425 the fracture network (Micklethwaite and Cox, 2004). The notion of repeated flow through
426 extensively interconnected crack networks in subducted slabs is consistent with the many
427 reports of hydrothermal veins in blueschists and eclogites. This fluid migration switches the
428 metamorphic regime from closed-system to open, changing the local fluid/rock ratio
429 throughout an affected rock volume.

430

431 In an open system where fluid is continually lost, as may be approached within
432 aseismically creeping domains, periods of increased anhydrite dissolution correspond to
433 chlorite and talc breakdown (Fig. 5A,B). Since metamorphic reactions that produce large
434 amounts of H₂O over small changes in *P* and *T* may promote increased seismic fracturing (cf.
435 Moreno et al., 2014), these regions in a given P-T diagram can be regarded as the primary
436 domains of seismic fracturing and fluid loss where the fluid mode will periodically reset to
437 nearly zero. On Figure 5C the effect of periodic fluid loss on anhydrite dissolution is
438 demonstrated for case where seismic rupture and fluid loss occurs when maximum fluid
439 production is reached during chlorite and talc breakdown. Figure 5 presents only two of an
440 infinite number of cases because seismic rupture may occur at any time, though more likely
441 when fluid liberation is high. Also shown on Figure 5 is the terminus of fluid liberation. If
442 fluid is lost through seismic processes, there can be no dissolution of anhydrite (or other
443 minerals) and only melt, or externally derived fluids, can mobilise material beyond this line.
444 This figure clearly shows that the blueschist–eclogite transition is the focus of fluid liberation
445 in the slab, and thus the focus of anhydrite dissolution.

446

447 In open systems, once fluids have escaped their source region, they can migrate rapidly
448 relative to metamorphic reaction rates, particularly when migration is fracture controlled such

449 as during an earthquake event. Structural heterogeneities like fractures and veins, which have
450 been shown to host anhydrite and barite in metasomatised oceanic crust and eclogites, are
451 expected to be the focus of earthquake-driven fluid egress from the slab. Sufficiently rapid
452 flow of externally-derived fluid through fractures would dissolve anhydrite without
453 equilibrating with minerals external to the vein (vein margins are the focus of repeated
454 rupturing in earthquake-related systems; e.g., [Micklethwaite and Cox, 2004](#)). In this scenario
455 the lack of equilibration would mean that anhydrite dissolution would be chemically isolated
456 from silicate-hosted ferrous iron, and thus produce predominantly sulfate species. Coexistence
457 with pyrite in the fracture would produce an H₂S-SO₂-bearing fluid, and anhydrite-pyrite-
458 magnetite would produce an H₂S-dominated fluid. Efficient extraction of sulfate-rich fluids in
459 an actively deforming slab environment could plausibly pump sulfate into the sub-arc mantle,
460 into positions where concurrent hydration and oxidation of peridotite could proceed.

461

462

463 **On the stability of pyrite**

464

465 The stability of pyrite in subducting oceanic crust is poorly constrained. In the continental
466 crust, pyrite break-down in mafic rocks occurs mainly at the transition from greenschist to
467 amphibolite facies ([Tomkins, 2010](#)); conditions where a significant proportion of
468 metamorphic H₂O is liberated from mainly chlorite. This results in liberation of H₂S into the
469 metamorphic fluid, which can then migrate upwards. However, the amount of H₂S
470 incorporated into the metamorphic fluid decreases significantly with increasing pressure
471 ([Tomkins, 2010](#)). Therefore, it might be expected that pyrite is a stable phase in the high
472 pressure environment of the blueschist and even lower eclogite facies.

473

474 Our observations show that, when shielded in garnet, pyrite survives well into the
475 eclogite facies. The textures in [Figure 6](#) suggest that pyrite reacted with bornite to form
476 sulfide melt. The phase relations in [Figure 7](#) indicate that the assemblage bornite + pyrite
477 would melt as temperatures approach 800°C. Although these phase relations are drawn for
478 atmospheric pressures, the temperature of sulfide melting typically increases by only a small
479 amount with increasing pressure ([Tomkins et al., 2007](#)). Nevertheless, this increase in
480 melting temperature with pressure indicates that sulfide melting reactions produce a volume
481 increase, so we interpret the radial bornite-filled fractures to have formed upon sulfide
482 melting; radial fractures typically surround inclusions that underwent a large volume increase
483 with respect to their host. Since the phase relations suggest temperatures approaching 800°C
484 – and this is consistent with independent thermometry for this region of $755 \pm 55^\circ\text{C}$ ([Zhang et](#)
485 [al., 2009](#)) – our interpretation is that pyrite was still present at these temperatures and had not
486 been converted to pyrrhotite. Thus, pyrite appears stable through the lower eclogite facies.

487

488 It may be that at higher pressures, a significant proportion of pyrite eventually breaks
489 down via reactions with ferromagnesian silicates (or Fe-bearing oxides):

490



492

493 This sort of reaction has been observed at many localities in the continental crust and
494 produces unusual Fe-depleted, Mg-, K- and Al-rich silicate bulk compositions in the vicinity
495 of highly metamorphosed sulfide mineral deposits (e.g., [Tomkins and Grundy, 2009](#)).
496 Whether this sort of reaction occurs in the subducted slab, or not, is important because it
497 causes both reduction and conservation of sulfur in the rock. If this happens in subduction
498 zones, then a large proportion of the sulfur budget would be recycled into the deep mantle as

499 pyrrhotite. Since our electron microprobe mapping detected no Fe depletion or zoning of any
500 sort in garnet immediately surrounding pyrite-free polymineralic sulfide inclusions from the
501 Sulu Belt, it is considered unlikely that new sulfide formed by sulfidation of garnet via pyrite
502 breakdown. This observation is consistent with preservation of pyrite in some inclusions and
503 lack of pyrrhotite.

504

505 Eclogite xenoliths in kimberlites, from regions of the mantle that experienced 1050°C,
506 typically contain pyrrhotite (Aulbach et al., 2012), so pyrite evidently transforms to
507 pyrrhotite at high temperatures. Our observations suggest that pyrite typically survives well
508 into the eclogite facies, well beyond the conditions where anhydrite would be dissolved in
509 metamorphic fluids. When pyrite does breakdown it may do so in relatively anhydrous rocks,
510 which would make egress of H₂S from the slab via locally generated hydrothermal fluid
511 difficult. In experiments investigating the behavior of sulfide during fluid-present melting of
512 basaltic slab, Jago and Dasgupta (2013) found that pyrite converted to pyrrhotite in all
513 experiments, which involved conditions as low as 800°C and 2.0 GPa (these experiments
514 were not buffered for f_{S_2} , and so would likely have lost sulfur from the experiment capsule,
515 thereby developing low f_{S_2} conditions, which render pyrite unstable). Slab melting, or
516 alternatively, development of highly solute-rich supercritical liquids (see Hermann et al.,
517 2006), requires addition of external fluids into the hotter slab top, most likely derived from
518 underlying devolatilising serpentinites (Spandler and Pirard, 2013). If such fluids were
519 sourced from pyrrhotite-bearing serpentinites, they would be expected to have low f_{S_2} and
520 thus be capable of driving pyrite breakdown. We therefore suggest that influx of serpentinite-
521 derived fluid causing slab melting and/or supercritical liquid development may be the more
522 likely mechanism for transfer of sulfide from the slab to the overlying mantle (cf. Jago and
523 Dasgupta, 2013; 2014).

524

525

526 **Separate zones of sulfate and sulfide release from subduction zones – consequences**

527

528 We suggest that sulfur liberation from a subducting slab may be initially oxidized,
529 involving input of sulfate into the mantle wedge through anhydrite break-down at the
530 blueschist-eclogite transition, and then reduced, resulting from pyrite break-down at
531 considerably higher P and T. We speculate that this zoned sulfur liberation might be one of
532 the factors that lead to the apparently redox-influenced zoned distribution of arc-hosted ore
533 deposits shown in [Figure 1](#).

534

535 In the trench-proximal part of the arc, it may be that reduction of fluid-bourn sulfate to
536 sulfide during metasomatism of the sub-arc mantle may be the main driver of oxidation of the
537 sub-arc mantle ([Evans and Tomkins, 2011](#)). Monosulfide solid solution (MSS) is the main
538 reservoir of chalcophile metals in the mantle, and these metals behave compatibly during
539 basalt generation as long as MSS remains in the residuum, so it might appear that melting
540 under MSS-stable conditions would inhibit formation of metal-rich basalts. However, given
541 that the solubility of monosulfide in basalt increases by an order of magnitude from
542 FMQ+0.5 to FMQ+1.5 (from ~1500 ppm to ~1.5%; [Jugo et al., 2010](#)), formation of melt in
543 mantle buffered at this oxidation state would result in a high degree of sulfide dissolution and
544 formation of a metal- and sulfur-rich magma at lower degrees of partial melting.

545

546 In more trench-distal parts of the arc, above the region where pyrite breaks down to
547 pyrrhotite, mantle metasomatism may be driven by infiltration of hydrous slab-derived
548 magmas or supercritical liquids (see [Jego and Dasgupta, 2013; 2014; Spandler and Pirard,](#)

549 2013). Here, there could plausibly be some oxidising effect on the mantle if the liquid/melt
550 source in the slab was significantly oxidised (Jego and Dasgupta, 2014) by the processes
551 detailed above. If not, H₂S can be transferred to the sub-arc mantle via fluid that coexists with
552 melt generated by water-saturated melting of the slab (Jego and Dasgupta, 2013), or via
553 supercritical liquid; magmas generated in such a region of metasomatised mantle would be
554 hydrous, reduced and sulfide-saturated. Upon reaching the base of the arc crust, some
555 magmas are thought to pond and partially crystallise. Because these magmas are likely to be
556 close to sulfide saturation, sulfides should exsolve after a small amount of crystallization,
557 sequestering chalcophile metals. Richards (2009) suggested that the deep-crustal residue of
558 partial crystallisation of arc basalt would be hydrous (mainly amphiboles) and sulfide-
559 bearing. He further suggested that remelting of such a residue during a subsequent
560 decompression event would lead to formation of gold-rich, low-sulfur magmas capable of
561 forming Au-rich magmatic-hydrothermal systems. Thus it may be that pyrite breakdown in
562 the slab has the potential to increase the metallogenic fertility of the sub-arc mantle,
563 enhancing the probability of forming Au-rich porphyry systems associated with reduced
564 magmas.

565

566 In Evans and Tomkins (2011) we suggested that sulfate transfer from the subducting slab was
567 the dominant agent responsible for sub-arc mantle oxidation during the Phanerozoic, whereas
568 the minimal sulfate in the deep oceans in the Pre-Ediacaran limited oxidative metasomatism
569 of the oceanic crust, and thus the arc magmatic system. It appears that pyrite still formed
570 during sea floor metasomatism in this earlier period since it is common in sea-floor
571 volcanogenic sulfide systems of this age. Therefore, we hypothesise that there could only
572 have been pyrite-associated desulfidation during slab subduction in the Proterozoic and
573 Archean. There may be several important consequences of a lack of anhydrite in subducting

574 oceanic crust during this period: (1) sulfur would only be added to the deeper parts of the
575 sub-arc mantle (i.e., only via pyrite breakdown); (2) given the relative insolubility of sulfide
576 in basaltic melt (Jugo et al., 2010), less sulfur could be recycled back into the crust above
577 subduction zones, and from there into the atmosphere (possibly influencing climate
578 variability over time); (3) the Pre-Ediacaran sub-continental lithospheric mantle keels may
579 thus have developed anomalous metallogenic fertility through less effective transferal of
580 sulfur and metal into the crust; (4) only ore systems associated with reduced magmas are
581 likely to have formed in arcs, such as reduced intrusion-related gold systems, which are
582 found in crust of this age; (5) more sulfur may have been recycled to the deep mantle in the
583 pre-sulfate period; and (6) modern subduction may not be an accurate representation of
584 earlier element recycling.

585

586

587 **Acknowledgements**

588

589 This research was supported through a Monash Research Accelerator grant to AGT, and an
590 ARC Future Fellowship to KAE. Professor Hongrui Fan is thanked for guidance during
591 fieldwork in the Sulu Belt. We thank Associate Editor Tim Elliot and an anonymous reviewer
592 for their constructive comments. This is TiGeR publication xxxx.

593

594

595 **References**

596

- 597 Alt, J.C., 1989. The geochemistry of sulfur in a 1.3 km section of hydrothermally altered
598 oceanic crust, DSDP Hole 504B. *Geochimica et Cosmochimica Acta* 53, 1011-1023.
599 Alt, J.C., 1995. Sulfur isotopic profile through the oceanic crust: Sulfur mobility and
600 seawatercrustal sulfur exchange during hydrothermal alteration. *Geology* 23, 585-588.
601 Alt, J.C., Laverne, C., Coggon, R.M., Teagle, D.A.H., Banerjee, N.R., Morgan, S., Smith-
602 Duque, C.E., Harris, M., Galli, L., 2010. Subsurface structure of a submarine

603 hydrothermal system in ocean crust formed at the East Pacific Rise, ODP/IODP Site 1256.
604 Geochemistry Geophysics Geosystems 11, Q10010.

605 Alt, J.C., Shanks, W.C., 2011. Microbial sulfate reduction and the sulfur budget for a
606 complete section of altered oceanic basalts, IODP Hole 1256D (eastern Pacific). *Earth and*
607 *Planetary Science Letters* 310, 73-83.

608 Aulbach, S., Stachel, T., Seitz, H.-M., Brey, G.P., 2012. Chalcophile and siderophile elements
609 in sulphide inclusions in eclogitic diamonds and metal cycling in a Paleoproterozoic
610 subduction zone. *Geochimica et Cosmochimica Acta* 93, 278-299.

611 Banno, S., Green, D.H., 1968. Experimental studies on eclogites: The roles of magnetite and
612 acmite in eclogitic assemblages. *Chemical Geology* 3, 21-32.

613 Barker, A.K., Coogan, L.A., Gillis, K.M., 2010. Insights into the behaviour of sulphur in mid-
614 ocean ridge axial hydrothermal systems from the composition of the sheeted dyke
615 complex at Pito Deep. *Chemical Geology* 275, 105-115.

616 Connolly, J.A.D., 2005. Computation of phase equilibria by linear programming: A tool for
617 geodynamic modeling and its application to subduction zone decarbonation. *Earth and*
618 *Planetary Science Letters* 236, 524-541.

619 Cotkin, S.J., 1987. Conditions of metamorphism in an Early Paleozoic blueschist, Schist of
620 Skookum Gulch, northern California. *Contributions to Mineralogy and Petrology* 96, 192-
621 200.

622 Cottrell, E., Kelley, K.A., 2011. The oxidation state of Fe in MORB glasses and the oxygen
623 fugacity of the upper mantle. *Earth and Planetary Science Letters* 305, 270-282.

624 Dale, J., Powell, R., White, R.W., Elmer, F.L., Holland, T.J.B., 2005. A thermodynamic
625 model for Ca-Na clin amphiboles in Na₂O-CaO-FeO-MgO-Al₂O₃-SiO₂-H₂O-O for
626 petrological calculations. *Journal of Metamorphic Geology* 23, 771-791.

627 Evans, K.A., Elburg, M.A., Kamenetsky, V.S., 2012. Oxidation state of subarc mantle.
628 *Geology* 40, 783-786.

629 Evans, K.A., Tomkins, A.G., 2011. The relationship between subduction zone redox budget
630 and arc magma fertility. *Earth and Planetary Science Letters* 308, 401-409.

631 Evans, K.A., Tomkins, A.G., Cliff, J., Fiorentini, M.L., 2014. Insights into subduction zone
632 sulfur recycling from isotopic analysis of eclogite-hosted sulfides. *Chemical Geology* 365,
633 1-19.

634 Faccenda, M., Gerya, T.V., Burlini, L., 2009. Deep slab hydration induced by bending-related
635 variations in tectonic pressure. *Nature Geoscience* 2, 790-793.

636 Frost, B.R., 1991. Stability of oxide minerals in metamorphic rocks. *Reviews in Mineralogy*
637 25, 469-488.

638 Fuhrman, M.L., Lindsley, D.H., 1988. Ternary feldspar modeling and thermometry. *American*
639 *Mineralogist* 73, 201-215.

640 Giacometti, F., Evans, K.A., Rebay, G., Cliff, J., Tomkins, A.G., Rossetti, P., Vaggelli, G.,
641 Adams, D.T., 2014. Sulfur isotope evolution in sulfide ores from Western Alps: Assessing
642 the influence of subduction-related metamorphism. *Geochemistry, Geophysics,*
643 *Geosystems* 15, 3808-3829.

644 Hannington, M.D., de Ronde, C.E.J., Petersen, S., 2005. Sea-floor tectonics and submarine
645 hydrothermal systems, *Economic Geology 100th Anniversary Volume 1905-2005.*
646 *Society of Economic Geologists, Littleton, Colorado* pp. 111-141.

647 Hermann, J., Spandler, C., Hack, A., Korsakov, A.V., 2006. Aqueous fluids and hydrous
648 melts in high-pressure and ultra-high pressure rocks: Implications for element transfer in
649 subduction zones. *Lithos* 92, 399-417.

650 Holland, H.D., Powell, R., 1996. Thermodynamics of order-disorder in minerals. 2:
651 symmetric formalism applied to solid solutions. *American Mineralogist* 81, 1425-1437.

652 Holland, T.J.B., Baker, J., Powell, R., 1998. Mixing properties and activity-composition
653 relationships of chlorites in the system MgO-FeO-Al₂O₃-SiO₂-H₂O. *European Journal of*
654 *Mineralogy* 10, 395-406.

655 Holland, T.J.B., Powell, R., 1998. An internally consistent thermodynamic dataset for phases
656 of petrological interest. *Journal of Metamorphic Geology* 16, 309-343.

657 Jago, S., Dasgupta, R., 2013. Fluid-present melting of sulfide-bearing ocean-crust:
658 Experimental constraints on the transport of sulfur from subducting slab to mantle wedge.
659 *Geochimica et Cosmochimica Acta* 110, 106-134.

660 Jago, S., Dasgupta, R., 2014. The fate of sulfur during fluid-present melting of subducting
661 basaltic crust at variable oxygen fugacity. *Journal of Petrology* 55, 1019-1050.

662 Jenner, F.E., O'Neill, H.S.C., Arculus, R.J., Mavrogenes, J.A., 2010. The magnetite crisis in
663 the evolution of arc-related magmas and the initial concentration of Au, Ag and Cu.
664 *Journal of Petrology* 51, 2445-2464.

665 Jugo, P.J., Wilke, M., Botcharnikov, R.E., 2010. Sulfur K-edge XANES analysis of natural
666 and synthetic basaltic glasses: Implications for S speciation and S content as function of
667 oxygen fugacity. *Geochimica et Cosmochimica Acta* 74, 5926-5938.

668 Kullerud, G., Yund, R.A., Moh, G.H., 1969. Phase relations in the Cu-Fe-S, Cu-Ni-S, and Fe-
669 Ni-S systems, in: Wilson, H.D.B. (Ed.), *Magmatic Ore Deposits*, pp. 323-343.

670 Lang, J.R., Baker, T., 2001. Intrusion-related gold systems: The present level of
671 understanding. *Mineralium Deposita* 36, 477-489.

672 Lee, C.-T.A., Luffi, P., Le Roux, V., Dasgupta, R., Albarède, F., Leeman, W.P., 2010. The
673 redox state of arc mantle using Zn/Fe systematics. *Nature* 468, 681-685.

674 Liu, Q., Frost, B.R., Wang, H., Zheng, J., Zeng, Q., Jin, Z., 2012. Magnetic petrology of high
675 Fe-Ti eclogites from the CCSG main hole: Implications for subduction-zone magnetism.
676 *Journal of Geophysical Research* 117, B07102.

677 Mallmann, G., O'Neill, H.S.C., 2009. The crystal/melt partitioning of V during mantle
678 melting as a function of oxygen fugacity compared with some other elements (Al, P, Ca,
679 Sc, Ti, Cr, Fe, Ga, Y, Zr and Nb). *Journal of Petrology* 50, 1765-1794.

680 McInnes, B.I.A., Gregoire, M., Binns, R.A., Herzig, P.M., Hannington, M.D., 2001. Hydrous
681 metasomatism of oceanic sub-arc mantle, Lihir, Papua New Guinea: Petrology and
682 geochemistry of fluid-metasomatised mantle wedge xenoliths. *Earth and Planetary*
683 *Science Letters* 188, 169-183.

684 Micklethwaite, S., Cox, S.F., 2004. Fault-segment rupture, aftershock-zone fluid flow, and
685 mineralization. *Geology* 32, 813-816.

686 Moreno, M., Haberland, C., Oncken, O., Rietbrock, A., Angiboust, S., Heidbach, O., 2014.
687 Locking of the Chile subduction zone controlled by fluid pressure before the 2010
688 earthquake. *Nature Geoscience* 7, 292-296.

689 Newton, R.C., Manning, C.E., 2005. Solubility of anhydrite, CaSO₄, in NaCl-H₂O solutions
690 at high pressures and temperatures: Applications to fluid-rock interaction. *Journal of*
691 *Petrology* 46, 701-716.

692 Okay, A.I., 1980. Sodic amphiboles as oxygen fugacity indicators in metamorphism. *Journal*
693 *of Geology* 88, 225-232.

694 Powell, R., Holland, T.J.B., 1999. Relating formulations of the thermodynamics of mineral
695 solid solutions: activity Ilmenite-hematite solid solution modelling of pyroxenes,
696 amphiboles and micas. *American Mineralogist* 84, 1-14.

697 Reinecke, T., 1998. Prograde high- to ultrahigh-pressure metamorphism and exhumation of
698 oceanic sediments at Lago di Cignana, Zermatt-Saas Zone, western Alps. *Lithos* 42, 147-
699 189.

700 Richards, J.P., 2009. Postsubduction porphyry Cu-Au and epithermal Au deposits: Products
701 of remelting of subduction-modified lithosphere. *Geology* 37, 247-250.

- 702 Richards, J.P., 2011. Magmatic to hydrothermal metal fluxes in convergent and collided
703 margins. *Ore Geology Reviews* 40, 1-26.
- 704 Spandler, C., Pirard, C., 2013. Element recycling from subducting slabs to arc crust: A
705 review. *Lithos* 170-171, 208-223.
- 706 Staudigel, H., 2003. Hydrothermal alteration processes in the oceanic crust, in: Rudnick, R.L.
707 (Ed.), *The Crust*. Elsevier-Pergamon, Oxford.
- 708 Tomkins, A.G., 2010. Windows of metamorphic sulfur liberation in the crust: Implications for
709 gold deposit genesis. *Geochimica et Cosmochimica Acta* Accepted subject to revision
710 (22/12/2009).
- 711 Tomkins, A.G., Grundy, C., 2009. Upper Temperature Limits of Orogenic Gold Deposit
712 Formation: Constraints from the Granulite-Hosted Griffin's Find Deposit, Yilgarn Craton.
713 *Economic Geology* 104, 669-685.
- 714 Tomkins, A.G., Pattison, D.R.M., Frost, B.R., 2007. On the initiation of metamorphic sulfide
715 anatexis. *Journal of Petrology* 48, 511-535.
- 716 Tomkins, A.G., Rebryna, K.C., Weinberg, R.F., Schaefer, B.F., 2012. Magmatic sulfide
717 formation by reduction of oxidised arc basalt. *Journal of Petrology* 53, 1537-1567.
- 718 Tsujimura, T., Kitakaze, A., 2004. New phase relations in the Cu-Fe-S system at 800°C;
719 Constraint of fractional crystallization of a sulfide liquid. *Neues Jahrbuch fur Mineralogie*.
720 *Monatshefte* 10, 433-444.
- 721 van Keken, P.E., Hacker, B.R., Syracuse, E.M., Abers, G.A., 2011. Subduction factory: 4.
722 Depth-dependent flux of H₂O from subducting slabs worldwide. *Journal of Geophysical*
723 *Research* 116, doi:10.1029/2010JB007922.
- 724 Zhang, R.Y., Iizuka, Y., Ernst, W.G., Liou, J.G., Xu, Z.-Q., Tsujimori, T., Lo, C.-H., Jahn,
725 B.-M., 2009. Metamorphic P-T conditions and thermal structure of Chinese Continental
726 Scientific Drilling main hole eclogites: Fe-Mg partitioning thermometer vs. Zr-in-rutile
727 thermometer. *Journal of Metamorphic Geology* 27, 757-772.

728
729

730 **Figure Captions**

731 **Figure 1** Distribution of mineral deposit types in the central Andean arc, showing that
732 trench-proximal deposits are dominated by porphyry Cu-(Au-Mo) and epithermal Au-Ag
733 systems, whereas trench-distal deposits are dominated by intrusion-related Au and Sb
734 systems.

735

736 **Figure 2** Schematic representation of sea floor sulfidation and oxidation associated with a
737 mid-ocean ridge.

738

739 **Figure 3** Phase relations for hydrated NMORB shown in A (composition in [Table 1](#)), with
740 contours of wt.% H₂O liberated through progressive metamorphism in B. Abbreviations:
741 amph = amphibole, chl = chlorite, coe = coesite, o = clinopyroxene, g = garnet, law =
742 lawsonite, opx = orthopyroxene, pl=plagioclase, q = quartz, ta = talc, zo = zoisite.

743

744 **Figure 4** Contours of anhydrite dissolution (g per kg of rock) involving slab-derived fluid
745 with 4 wt.% NaCl (A) and 10 wt.% NaCl (B), based on the H₂O liberation data given in
746 [Figure 3B](#). The hot and cold geotherms are for slab moho, from [van Keken et al. \(2011\)](#).

747

748 **Figure 5** The effect of open system fluid egress on anhydrite dissolution. A. On the cold
749 geotherm H₂O liberation is related to chlorite breakdown and talc breakdown is not reached

750 at the conditions investigated. All of the anhydrite dissolution, in this case for 10 wt% NaCl
751 in the fluid, is thus related to the chlorite-derived H₂O, and because the system is open,
752 anhydrite dissolution ceases at the chlorite-out line. B. On the hot geotherm there are two
753 pulses of anhydrite dissolution related to chlorite and then talc breakdown, with a minor
754 contribution from lawsonite breakdown at higher T. At these hotter, lower pressure
755 conditions the effects of open system fluid loss on anhydrite dissolution are more pronounced
756 (calculations for 10 wt% NaCl). C. In these models for 4 and 10 wt% NaCl on the hot
757 geotherm, the fluid is allowed to stay in the rock until the chlorite-out line when all fluid is
758 extracted, then fluid is allowed to rebuild until the talc-out line when fluid is extracted again.
759 These models represent a periodically open system where earthquake events occur at times of
760 extensive fluid generation, allowing development of fracture connectivity and fluid egress.

761

762 **Figure 6** Sulfide inclusions in a 10 cm garnet porphyroblast from coesite-bearing mafic
763 eclogite in the Sulu Belt, China (N37° 06' 58.4", E122° 18' 03.6"). A and B: A hexagonal
764 pyrite-bornite inclusion with fine peripheral fractures coated with bornite. In the EMP
765 element map, B, yellow highlights the distribution of Cu, and blue highlights the distribution
766 of Co in zoned pyrite, reflecting variations in fluid chemistry during pyrite formation. C and
767 D: EMP element maps showing hexagonal inclusions of primary Cu-Ni sulfides in garnet.
768 The distribution of iron in garnet is highlighted in green (in C) and blue (in D), showing no
769 zonation with respect to the sulfide inclusion.

770

771 **Figure 7** Phase relations in the system Cu-Fe-S between 700 and 800°C. The 700°C
772 diagram is from [Kullerud et al. \(1969\)](#), the 800°C diagram is from [Tsujimura and Kitakaze \(2004\)](#).
773 The diagrams show the phase relations at atmospheric pressure, whereas contrary to
774 the 700°C section, our observations indicate that pyrite and bornite can coexist at subduction
775 zone pressures and elevated temperatures, prior to melting. Abbreviations: Py = pyrite, Po_{ss} =
776 pyrrhotite solid solution, Bn_{ss} = bornite solid solution, iss = intermediate solid solution.

777

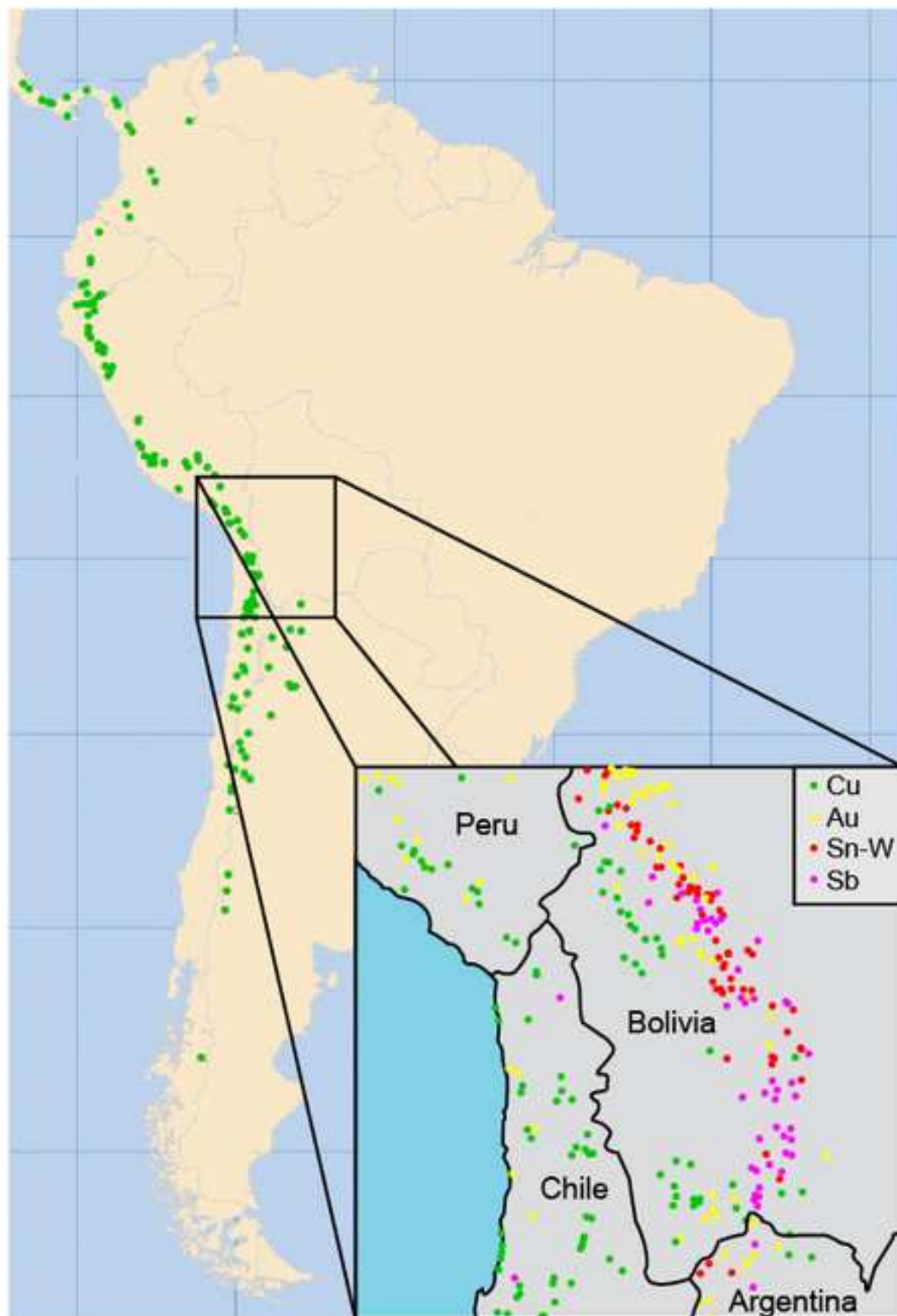
Highlights

- Anhydrite primarily breaks down across the blueschist–eclogite transition.
- Pyrite is stable in the lower eclogite facies up to at least 750°C.
- Two zones of sulfur liberation from the slab are likely.
- Sulfate is released closer to the trench, sulfide more distally.

Figure

[Click here to download high resolution image](#)

Figure 1 - Tomkins & Evans



Figure

[Click here to download Figure: Fig2 Seafloor Alteration.eps](#)

Figure 2 - Tomkins & Evans

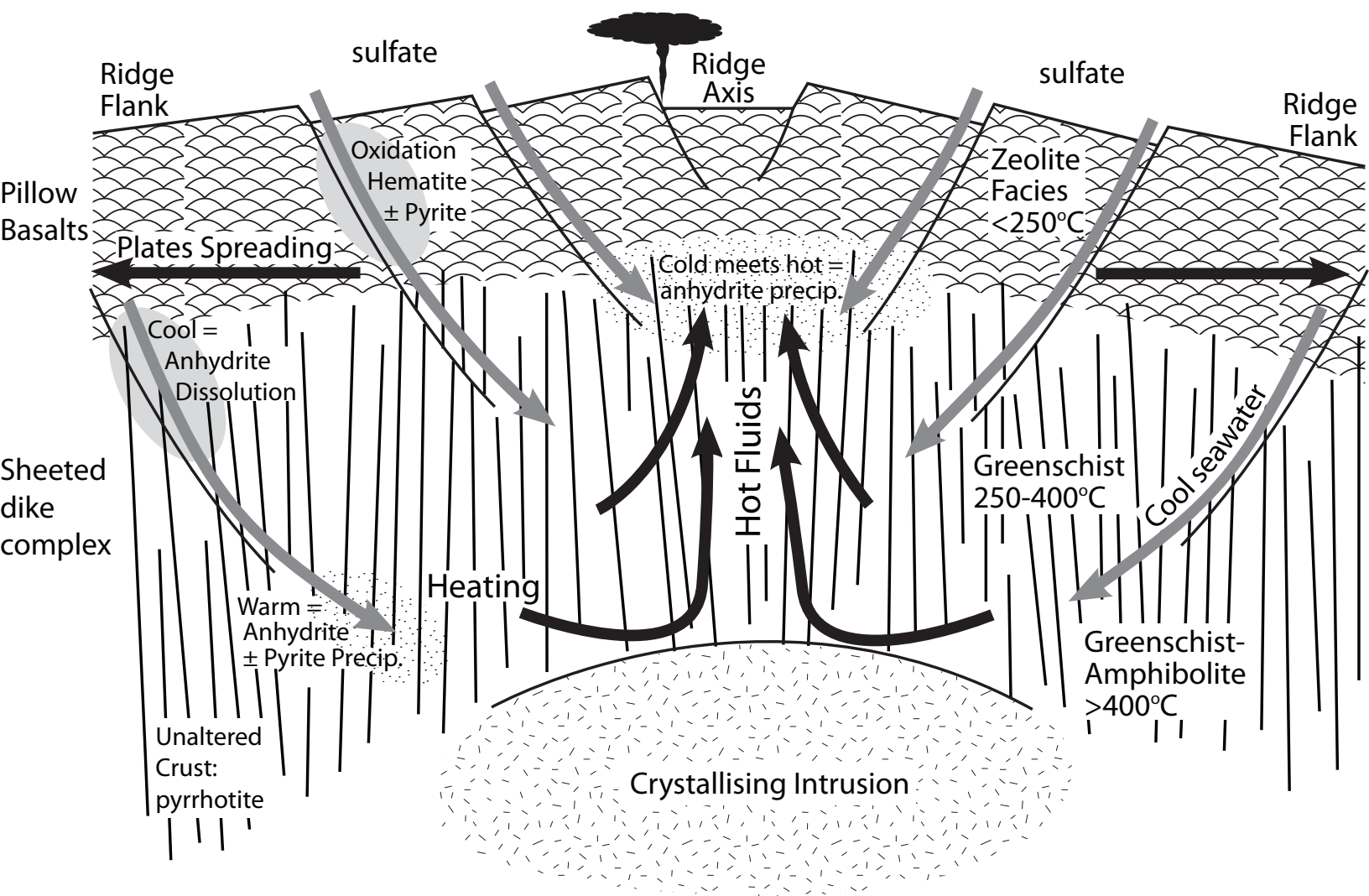


Figure
[Click here to download Figure: Fig3 H2O release.eps](#)

Figure 3 - Tomkins & Evans

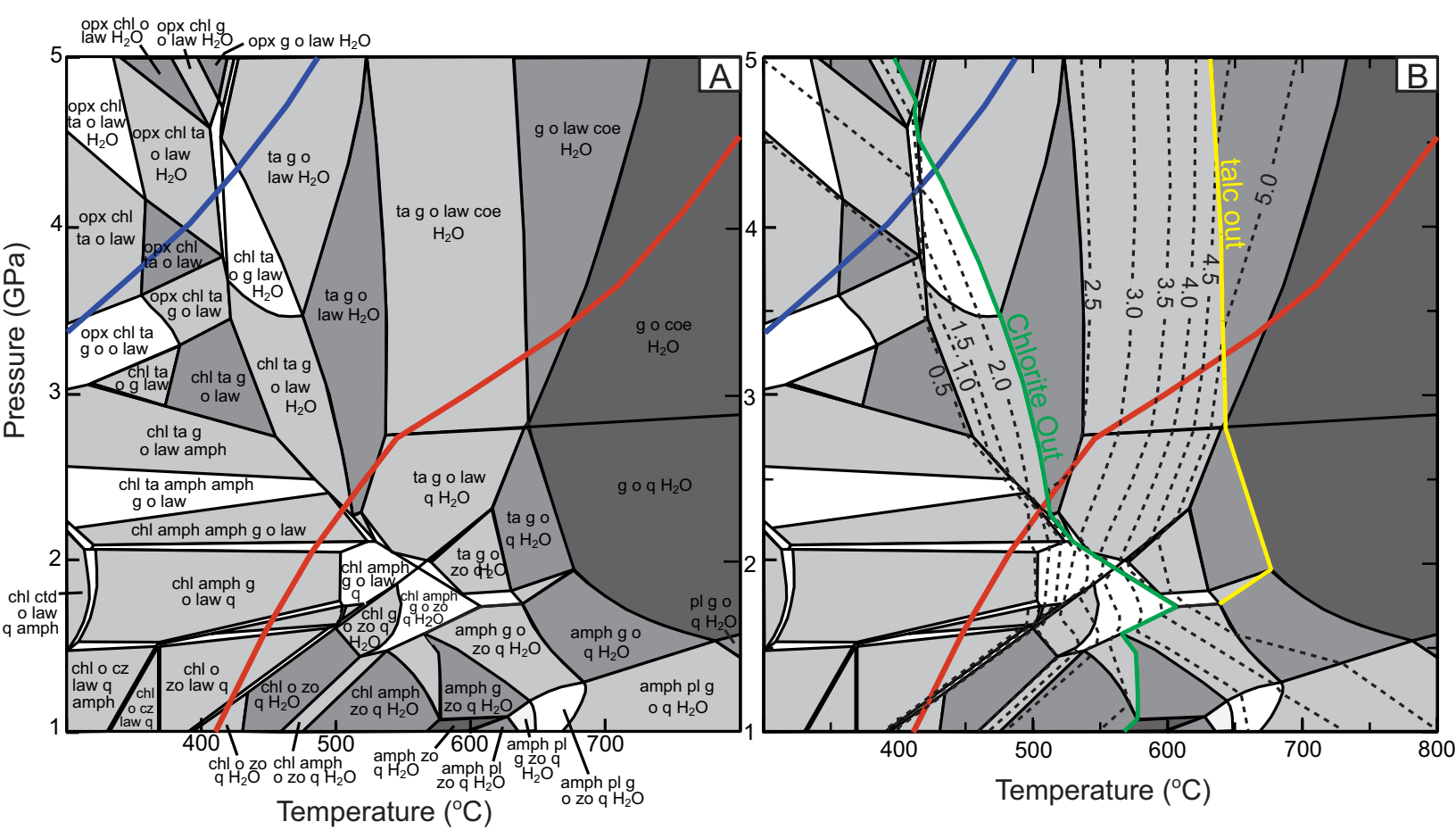
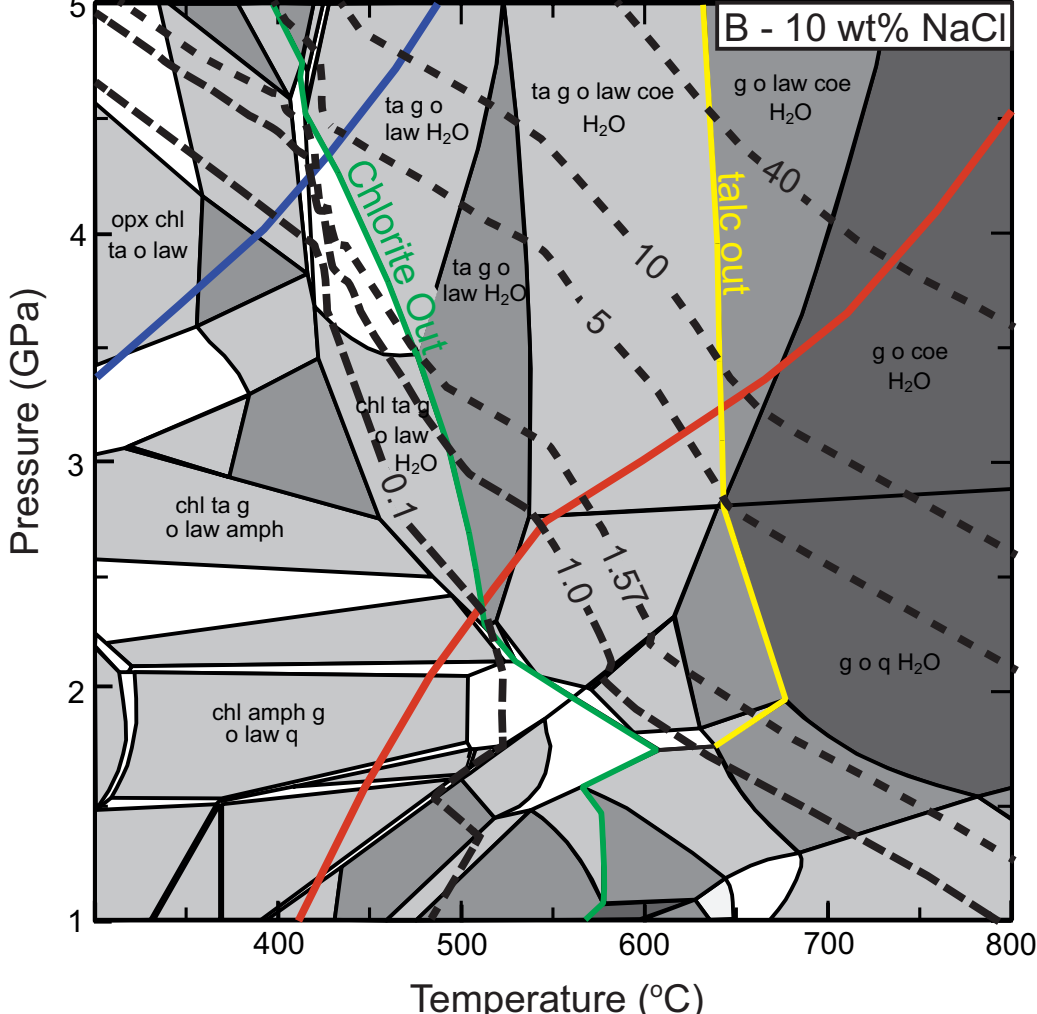
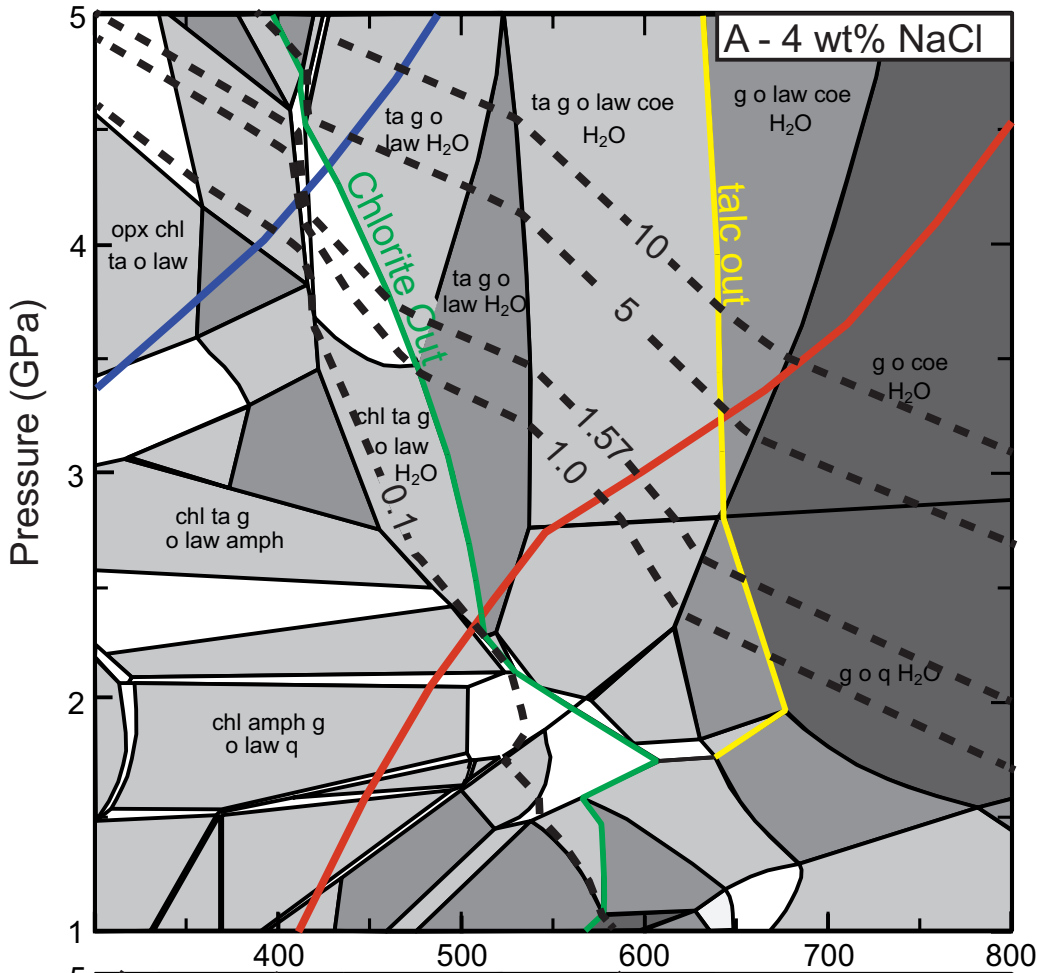


Figure 4 - Tomkins & Evans
[Click here to download Figure: Fig4 Anhydrite contours.eps](#)



Figure[Click here to download Figure: Fig5 open closed.eps](#)

Figure 5 - Tomkins & Evans

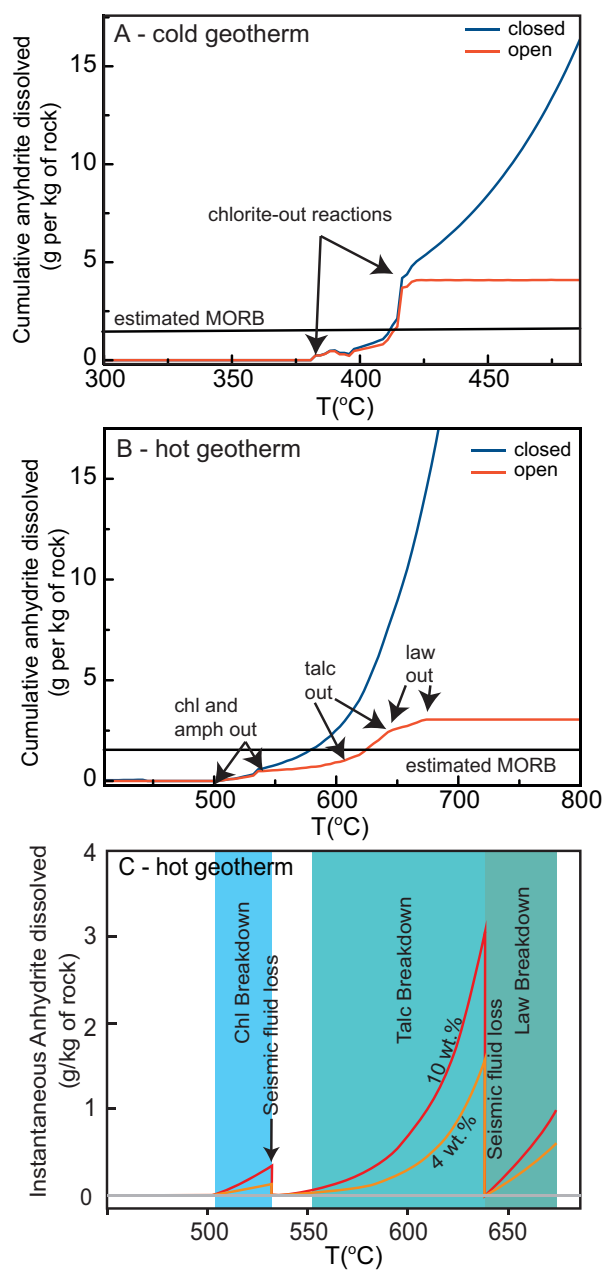


Figure 4 - Tomkins & Evans

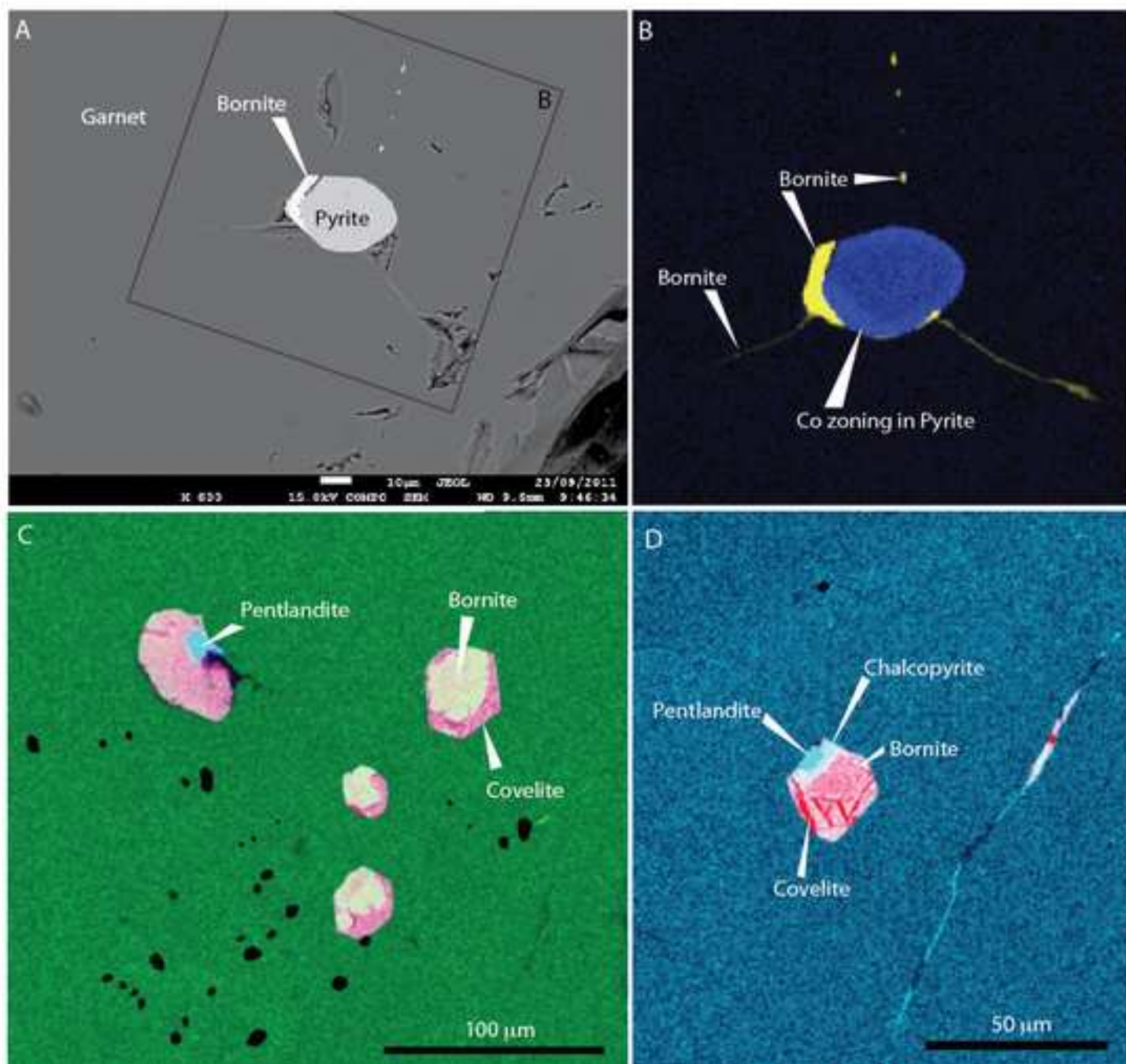


Figure 7 - Tomkins & Evans

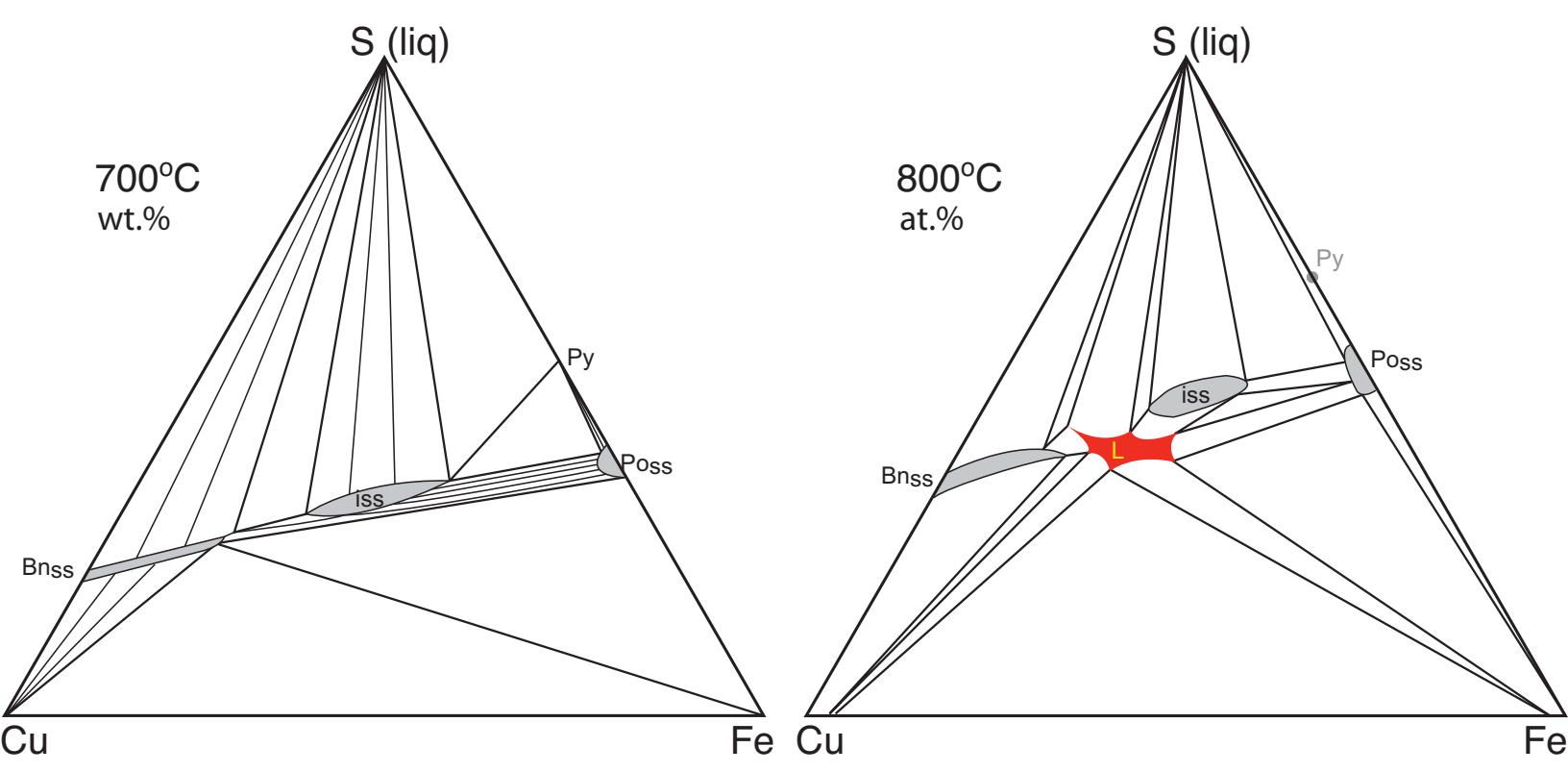


Table 1. Composition of modelled N-MORB.

Oxide	Concentration (wt%)
SiO ₂	47.99
Al ₂ O ₃	15.65
MgO	8.32
FeO	9.34
CaO	11.28
Na ₂ O	2.42
H ₂ O	5